





Exploiting the two-dimensional magneto-optical trapping of ^{199}Hg for a mercury optical lattice clockChanglei Guo , Valentin Cambier *, James Calvert , Maxime Favier, Manuel Andia ,
Luigi de Sarlo, and Sébastien Bize*LNE-SYRTE, Observatoire de Paris, Université PSL, CNRS, Sorbonne Université, 61 Avenue de l'Observatoire, 75014 Paris, France*

(Received 4 July 2022; revised 13 January 2023; accepted 13 March 2023; published 27 March 2023)

Two-dimensional magneto-optical trapping (2D-MOT) is an efficient tool for generating a high flux of precooled atoms. A 2D-MOT for mercury (Hg) is so far missing despite the potential of this atomic species in several areas. Here, we present the characterization of a 2D-MOT for Hg enabled by addressing the 1S_0 - 3P_1 laser cooling transition at 254 nm. The laser source based on an ytterbium-doped fiber amplifier has low-frequency noise and high reliability. Parameters affecting the efficiency of the 2D-MOT are studied, i.e., optical trapping power, push beam power, cooling laser frequency detuning, and magnetic-field gradient. When used with a Hg optical lattice clock, the 2D-MOT increases by a factor of 4.5, the rate of preparation of the atomic samples, yielding an improved clock short term stability of 6.4×10^{-16} at 1 s.

DOI: [10.1103/PhysRevA.107.033116](https://doi.org/10.1103/PhysRevA.107.033116)**I. INTRODUCTION**

Efficient sources of cold atoms are an essential tool for a wide range of experiments, such as quantum gases [1], atom-based sensors [2–5], and fundamental and applied investigations based on atomic and molecular spectroscopy [6,7]. Two-dimensional magneto-optical trapping (2D-MOT) is one of the most compact and effective schemes to provide a high-flux cold atom beam. The scheme was demonstrated and used with alkali atoms [8] and then extended to other atomic species, namely, alkaline-earth-like atoms. 2D-MOT with Yb and Sr are used in the context of quantum gases and clock experiments [9–12]. Mercury (Hg) is an alkaline-earth-like atom which exhibits promising properties to realize an optical lattice clock with high reproducibility and accuracy owing to its low sensitivity to black-body radiation [13,14]. A source chamber of mercury needs a cooler rather than an oven to tune the desired vapor pressure due to its intrinsic high-vapor-pressure property. Moreover, this property makes it avoid using Zeeman slower as is necessarily used in Yb or Sr apparatus, which, in turn, makes the whole vacuum system simple and compact. Even though Hg is studied in the laser-cooled regime by several groups [15–20], a 2D-MOT of Hg is so far missing despite the potential of this atomic species in several areas.

A 2D-MOT for Hg has been briefly applied in our Hg experiment in early investigations [13]. However, the poor reliability and power of 254-nm laser technologies available at the time prevented the further use of this 2D-MOT for the development of a Hg optical lattice clock. Also, studying and characterizing the 2D-MOT was not possible. In this article, we demonstrate the 2D-MOT for Hg enabled by a dedicated 254-nm laser system based on ytterbium-doped fiber amplifiers (YDFAs) [21]. We first describe the vacuum apparatus where Hg is laser cooled. We then describe the deep-UV

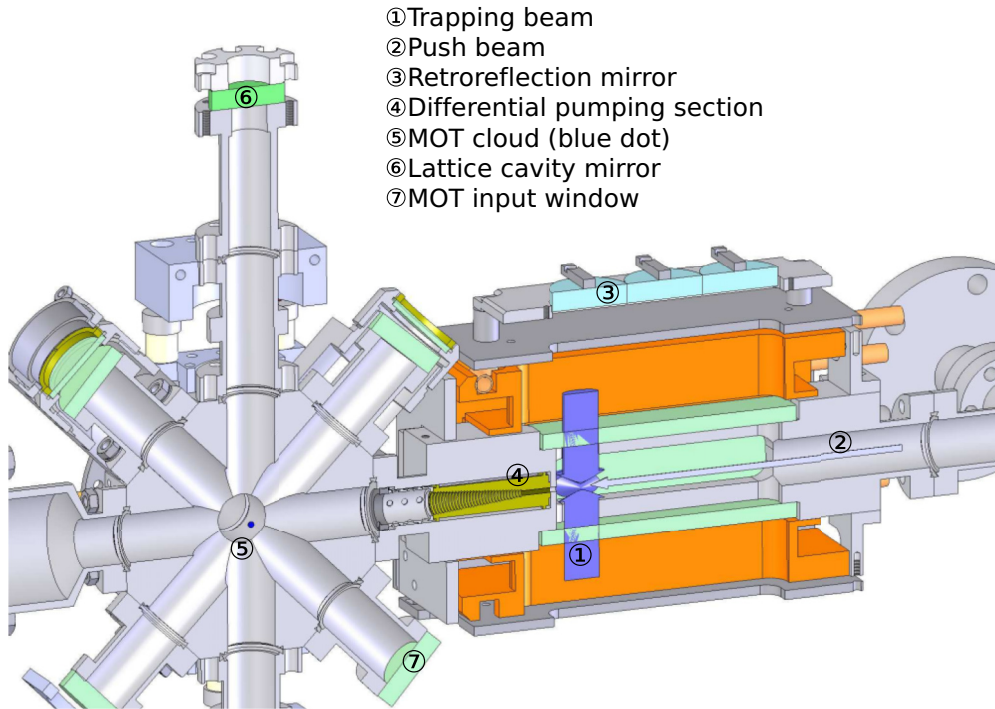
laser systems and their intensity and frequency characteristics, which are the prerequisites for laser cooling. Third, we emphasize the description, optimization, and characterization of the 2D-MOT enabled by the novel laser sources. Finally, we report an improvement of the frequency stability of our Hg optical lattice clock (Hg clock) when it exploits the increased cold atom flux obtained from the 2D-MOT, and, as a consequence, an improved duty cycle for the clock.

II. EXPERIMENTAL APPARATUS

The apparatus with 2D-MOT and 3D-MOT including a lattice cavity used in the experiment is shown in Fig. 1. A few grams of Hg are held in a source chamber connected to the 2D-MOT chamber (the connector is shown on the right side in Fig. 1) where the Hg is cooled down approximately to -40°C . This provides a vapor pressure of $\sim 10^{-4}$ Pa in the source chamber [22]. The details of the source chamber are described and discussed in Ref. [23]. The 2D-MOT trapping beams and the push beam are represented with arrows in the figure. Our design uses rectangular windows where we arrange three trapping zones defined by three sets of input mirrors, $\lambda/4$ wave plates, and retroreflection mirrors. So far, only the trapping zone closest to the 3D-MOT is used. Two pairs of anti-Helmholtz coils are used to generate the required magnetic-field gradient. The connection between the 3D-MOT and the 2D-MOT is a differential pumping section, which is a 1.5-mm diameter, 10-mm long tube ending in a threaded gold-coated conic output [13]. The push beam size is also optimized, which is less than 1 mm in diameter in the trapping zone.

The cold Hg atoms are obtained by exciting the 1S_0 to 3P_1 cooling transition [13,14,24] at 254 nm, which has a linewidth of $\gamma \approx 1.3$ MHz. This provides an efficient and simple scheme for cooling Hg to tens of microkelvins using a single-wavelength laser (no need for two-stage cooling) [15]. The schematic of the whole laser systems is shown in Fig. 2. There are two separate UV generation lines to drive the

*Corresponding author: valentin.cambier@obspm.fr



- ① Trapping beam
- ② Push beam
- ③ Retroreflection mirror
- ④ Differential pumping section
- ⑤ MOT cloud (blue dot)
- ⑥ Lattice cavity mirror
- ⑦ MOT input window

FIG. 1. The apparatus with 2D-MOT and three-dimensional (3D)-MOT including a lattice cavity. The trapping beams (thick blue arrows) are labeled as 1, whereas the push beam (thin gray arrow) is labeled as 2. Other parts are also labeled and listed in the figure.

3D-MOT and the 2D-MOT, respectively. To meet the requirement of narrow linewidth of cooling transition, two homemade single-frequency external cavity diode lasers (Seed 1 and Seed 2) are designed with 12-cm long external cavities. In the 3D-MOT subsystem, the output power of Seed 1 is first amplified by YDFA 1. Then, it is frequency doubled to 507.5 nm by second harmonic generation through a single-pass frequency doubling unit (periodically poled-lithium tantalate,). The 254-nm laser is finally realized

through the subsequent homemade bow tie doubling cavity (angle-tuned BBO) [25]. The maximum UV output power can be more than 150 mW. The final output power from the cavity can be tuned and controlled by side locking of the cavity resonance to the 254-nm light. This provides a means to set the output power to the desired value. Part of the 254-nm light from the UVC 1 is sent to a Hg cell for accurate frequency locking based on the saturated-absorption-locking method. AOM 1 and AOM 2 are used in the frequency lock-

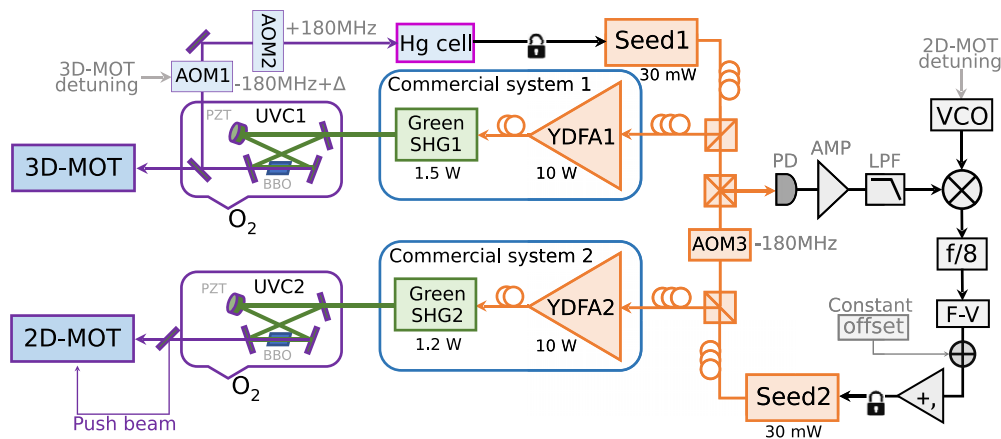


FIG. 2. Schematic of the MOT laser subsystems. YDFA; SHG: second harmonic generation; UVC: UV cavity; AOM: acousto-optic modulator; PD: photodiode; AMP: amplifier; LPF: low-pass filter; VCO: voltage-controlled oscillator; $f/8$: frequency divider; F-V: frequency-to-voltage converter; PI: proportional-integral controller. The YDFAs and the subsequent SHG units are from commercial systems (Azurlight Systems). The UV lasers are generated in bow tie shape cavities by using γ -barium borate (BBO) crystals. Part of the UV light from the first UV cavity (UVC1) is sent to a Hg cell for absolute frequency locking where the 3D-MOT detuning is controlled by AOM 1. Two seed lasers are locked with the help of a F-V converter (AD590, the input frequency is ~ 350 kHz). The 2D-MOT detuning is controlled by tuning the VCO frequency. The respective optical power of a seed laser, YDFA, and SHG is labeled.

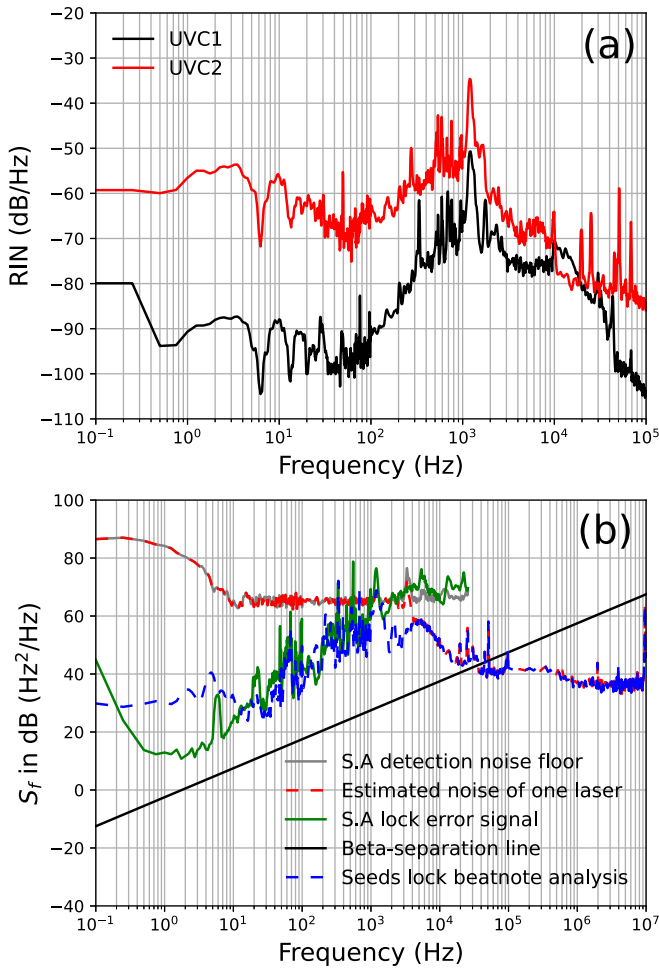


FIG. 3. (a) Relative intensity noise (RIN) at 254 nm in UVC 1 and UVC 2, respectively. (b) Frequency noises at 254 nm inferred from the error signal of the saturated absorption (S.A.) lock (green) from the detection noise of this lock (gray) and from the beat note between the two seed lasers (blue), respectively. The estimated noise of one UV laser (red dashed line) uses combined data from these curves and other information, such as servoloop bandwidths. The β -separation line is used for laser linewidth estimation [26].

ing loop, where AOM 1 is used to set the detuning for the 3D-MOT.

The 2D-MOT subsystem is mostly similar to the former. In order to copy the laser frequency from Seed 1 to Seed 2, a frequency lock unit based on a F-V converter is built where the frequency beat note (detected by photodiode, and processed by rf amplifier and low-pass filter) between Seed 1 and Seed 2 are mixed with a VCO working around 180 MHz. The mixed frequency passes through a $f/8$ frequency divider before being converted to a direct voltage. It is subsequently subtracted from a constant voltage offset and sent to the PI controller. Finally, the servoloop is closed by feeding back to the piezoactuator mirror in Seed 2. The detuning between Seed 1 and Seed 2 is controlled by tuning the VCO frequency. In this way, we can control the 2D-MOT detuning accordingly.

The intensity and frequency noise characterization of the laser systems are shown in Figs. 3(a) and 3(b), respectively. As shown in Fig. 3(a), the RIN profiles of both 254-nm lasers

are not overlapped even though they share some similar noise peaks. The RIN in UVC 2 is much higher than that in UVC 1 at the low-frequency part. We attribute this difference to the fact that the two UV cavities are not identically designed (different mechanical design, different cavity length, different beam size hitting on the BBO crystal, etc.) even though they are using the similar configuration (bow tie shape cavity). The much higher RIN in UVC 2 might come from some acoustic modes of the mechanical structures in it, which are still not fully understood. A similar lock kit (proportional-integral-derivative loop) as used for UVC 1 will not kill the extra RIN in UVC 2. The RINs of the two UV lasers are indeed not as good as some outstanding lasers. However, the -90 dB/Hz RIN for Fourier frequency of 1 Hz in UVC 1 is good enough for atom-trapping application in our clock system because the optical power fluctuations induce negligible fluctuations in the number of cold atoms.

Reaching the lowest temperature of the atomic samples requires a laser linewidth not higher than a small fraction of the natural linewidth. Here, this sets a fairly stringent requirement to have a laser linewidth no more than a few 100 kHz at 254 nm. Figure 3(b) shows frequency noises in the laser systems. The green, gray, and blue curves represent frequency noises at 254 nm inferred from the error signal of the S.A. lock, from the detection noise of this lock and from the beat note between the two seed lasers, respectively. Because both servoloops have bandwidths of near 3 kHz, the two seed lasers have their free running characteristics for Fourier frequencies much greater than 3 kHz. Given the identical realization of the two seed lasers, it is reasonable to assume that, in this high-frequency range, they have identical and uncorrelated contributions to the beat note noise. At Fourier frequencies much lower than 3 kHz, servoloop of Seed 1 copies the detection noise of the S.A. lock. In order to have a smooth transition between the low- and high-frequency region around 3 kHz, we used a normalized function Eq. (1) to produce the red dashed curve in Fig. 3(b). Here, f_c is the transition frequency (here it is the servoloop bandwidth of 3 kHz), \mathcal{W} (width) is a parameter used to tune the slope of the transition region, and PSD_1 and PSD_2 are the frequency noises of the gray and blue curves, respectively. With these curves, we can apply the β -separation line method [26] to derive the single laser linewidth, which is ~ 330 kHz with $\mathcal{W} = 1$ kHz. We also performed extreme estimations by tuning \mathcal{W} , and the lower and upper bounds of the linewidth estimations are 270 and 420 kHz, respectively. It is, thus, believed that the UV laser linewidth fits the requirement for efficient laser cooling of atomic samples.

$$\text{PSD} = \left\{ \frac{1}{2} \left[1 - \tanh \left(\frac{f - f_c}{\mathcal{W}} \right) \right] \right\}_{\text{norm}} \text{PSD}_1 + \left\{ \frac{1}{2} \left[1 + \tanh \left(\frac{f - f_c}{\mathcal{W}} \right) \right] \right\}_{\text{norm}} \text{PSD}_2. \quad (1)$$

III. CHARACTERIZATION OF THE 2D-MOT

To characterize the 2D-MOT, four parameters, namely, the total UV laser trapping power, push beam power, laser detuning, and magnetic-field gradient, are separately tuned

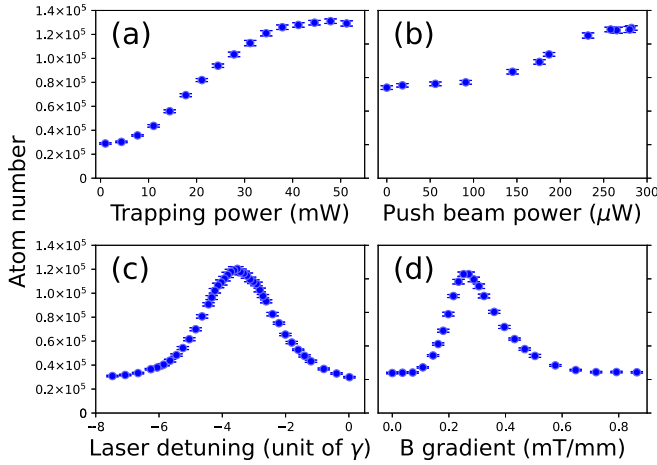


FIG. 4. Characterization of the 2D-MOT. Atom number in the 3D-MOT measured with varying (a) 2D-MOT trapping power (push beam power is 0.8% of the trapping power); (b) push beam power; (c) laser detuning in units of γ (1.3 MHz); and (d) magnetic-field gradient. Only one parameter is changed in each curve. The 3D-MOT parameters are with 220-ms MOT duration time and 25.9-mW UV trapping power.

as shown in Fig. 4, where the trapped atom numbers in the 3D-MOT are recorded using a fluorescence detection method from a calibrated CCD camera. To find the global optima of the parameters, several rounds of iterations have been performed. In each characterization, only one parameter is varied, and the other parameters are kept at their respective optima as shown in Fig. 4. The 3D-MOT parameters are fixed with 220-ms MOT duration time and 25.9-mW UV trapping power ($\sim 12 \times 12$ -mm² beam size). Such duration time is chosen to guarantee the shortest duty cycle as possible for the clock whereas keeping a significant atom flux to improve the clock stability (more details are given in Sec. IV). First, the total UV power at 254 nm for both trapping and pushing is changed by setting the power lock point of UVC 2. The push beam power is kept at 0.8% of the trapping power. As shown in Fig. 4(a), with increasing the UV power at 254 nm, the trapped atomic population is increased from 3.0×10^4 to 1.3×10^5 . After 40 mW, the total trapped atomic population is going to saturation (a saturation of the 3D-MOT loading, and not of the trapping transition itself). This is mainly limited by the beam size ($\sim 3 \times 9$ mm²) used in the 2D-MOT. An enlarged beam size is expected to further increase the trapped atomic numbers with increased UV power in the future. Second, the push beam power alone is varied as shown in Fig. 4(b). The trapped atomic population is increased from 7.6×10^4 to 1.26×10^5 (gain of 65%) by increasing the push beam power from zero to more than 250 μ W where the 2D-MOT trapping power is kept at 34.5 mW. The saturation effect is also seen here after 250 μ W. In the end, laser detuning and magnetic-field gradient in the 2D-MOT are tested as shown in Figs. 4(c) and 4(d), respectively. Optima of -3.5γ and 0.26 mT/mm are observed in our typical configurations.

A first benefit from the 2D-MOT is the increased MOT-loading rate. This means to reach the same trapped atom numbers in the MOT, a shortened MOT-duration time is

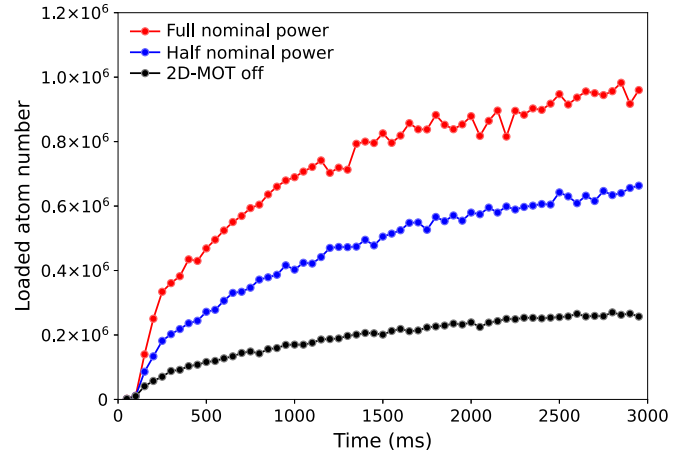


FIG. 5. MOT-loading curves with different UV trapping powers in the 2D-MOT. The nominal trapping power for the 2D-MOT is ~ 34.5 mW. The 3D-MOT parameters are the same as the ones in Fig. 4.

expected. Figure 5 shows the MOT-loading curves with different UV powers in the 2D-MOT, i.e., 2D-MOT off, half-nominal trapping power, and full-nominal trapping power (~ 34.5 mW), respectively. In the case of our typical 220-ms MOT-duration time, the trapped atomic numbers in the 3D-MOT are 0.06×10^6 , 0.15×10^6 , and 0.28×10^6 , respectively. If we assume the MOT loading has linear character with the duration time, we have MOT-loading rates of 0.28×10^6 , 0.68×10^6 , and 1.27×10^6 atoms/s, respectively. We, thus, have a gain factor of more than 4.5 of the MOT-loading rate. From the three curves, we determine MOT-loading time constants, which are 1.09 ± 0.05 s (black), 1.07 ± 0.04 s (blue), and 0.76 ± 0.04 s (red), respectively, with a model of $y = a \exp(-t/\tau) + b$, where τ is the time constant. Note when the trapping power is changed, the push beam power is simultaneously changed proportionally as mentioned earlier. When shutting off the push beam, we found the MOT-loading constants can be recovered to similar values as those without the 2D-MOT. This indicates it is the push beam that changes MOT-loading constants significantly. We attribute this to the fact that the push beam introduces a perturbation when it propagates all the way close to the 3D-MOT region that cannot be completely avoided. However, this makes no significant effect when the MOT-loading duration is short as in our case (typically 220 ms) and, thus, does not raise a problem. We also tested the 2D-MOT with lowered vapor pressure in the source chamber. The MOT-loading rates decrease and the MOT-loading time constants increase (up to 2.3 s) as similar as the results in Ref. [22]. However, the gain coefficient of the atom loading rate thanks to the 2D-MOT does not change significantly.

IV. CLOCK STABILITY MEASUREMENT WITH THE 2D-MOT

A clock stability model shown in Eq. (2) is built to analyze the clock stability [27]. f_{Hg} is the Hg clock transition frequency, \mathcal{S} is the slope of atomic spectroscopy signal at the

lock point (in units of 1/Hz), N_{at} is the atomic number for interrogation, η_{ph} is the detected photon number per atom, δ_N is the uncorrelated root-mean-squared fluctuation of the atom number during the detection, γ is the frequency noise induced by the probe laser due to the Dick effect [28,29], T_c is the clock cycle time (which includes the MOT-duration time T_{MOT} , the atomic interrogation T_R , and other clock sequence time T_S , $T_c = T_{\text{MOT}} + T_R + T_S$), and τ is the integration time. Before the availability of our 2D-MOT, we typically used to run our Hg clock with a cycle time over 1 s, and the best short-term stability of the clock was $1.2 \times 10^{-15}/\sqrt{\tau}$ [25]. The duty cycle (fraction of time spent on probing the clock transition) for atomic interrogation with the Rabi π pulse was less than 10%. As a consequence, the clock stability was highly hindered by the Dick effect. By exploiting the 2D-MOT, we, thus, expect a better clock stability from shortening the clock cycle time, and from reducing the Dick effect,

$$\varsigma = \sqrt{\left(\frac{1}{f_{\text{Hg}} \times S}\right)^2 \left[\frac{1}{N_{\text{at}}} + \frac{1}{N_{\text{at}}\eta_{\text{ph}}} + \frac{2\delta_N^2}{N_{\text{at}}^2}\right] + \gamma^2 \sqrt{\frac{T_c}{\tau}}}. \quad (2)$$

To demonstrate this improvement, the Hg clock stability was tested by interrogating a single Zeeman component of ^{199}Hg (i.e., $|^1S_0, m_F = 1/2\rangle \rightarrow |^3P_0, m_F = 1/2\rangle$). Figure 6(a) shows a typical atomic spectroscopy signal measurement (transition probability, blue dots) using a Rabi π pulse with a length of 160 ms. The MOT duration is once again fixed at 220 ms, the clock cycle time is ~ 482 ms, which gives a duty cycle of 33%. The lattice trap depth is $\sim 70 E_{\text{rec}}$ (recoil energy) with the magic wavelength maintained using a method demonstrated in Ref. [30]. The normalized detection method for measuring the transition probability and the complete clock sequence is described in Refs. [31,32]. From Fig. 6(a), one can see that the transition probabilities sit on a significant background which is mainly attributed to the limited lifetime of the Hg atom in the lattice trap (typically 300 ms) and the limited 3P_0 lifetime of the ^{199}Hg atom itself. The red solid line is a fit using a typical Rabi transition model, which gives us the S information used for closing the clock loop and for estimating the clock stabilities (as will be shown later).

The gray squares in Fig. 6(b) are a typical overlapping Allan deviation (OADEV) analysis based on the frequency corrections of the servoloop that locks the probe laser frequency to the atomic transition. This OADEV quickly reaches the flicker floor of our ultrastable laser determined by the ultracompact reference cavity used here, which is approximately 4.0×10^{-16} [33]. Since we do not have a better counterpart (a better clock or better interrogation laser) to compare to, we resort to use another provisional indicator. The transition probabilities are recorded during the operation of the clock. These transition probabilities are converted to frequencies based on S . In the case of Fig. 6(a), this signal has a given S of $\sim \pm 0.1/\text{Hz}$ around the two lock points. The OADEV analysis based on the frequency samples obtained by these means is shown as black solid dots in Fig. 6(b). The first point provides an evaluation of the short-term stability, which gives a value of $6.4 \times 10^{-16}/\sqrt{\tau}$.

In order to confirm this stability, the parameters $f_{\text{Hg}} = 1.129 \text{ PHz}$, $S = 0.1/\text{Hz}$, $N_{\text{at}} \approx 1700$, $\eta_{\text{ph}} = 0.7$, $\delta_N = 100$,

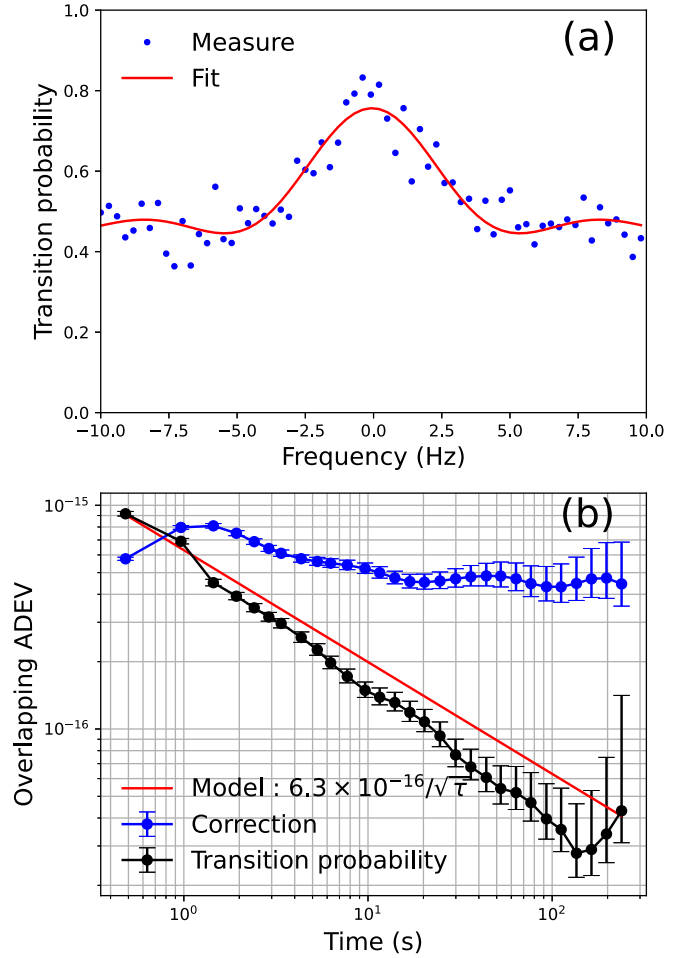


FIG. 6. Characterization of the Hg clock with the 2D-MOT. (a) A typical atomic spectroscopy signal measurement (transition probability, blue dots) using a Rabi- π pulse with a length of 160 ms. The red solid line is a fit using a typical Rabi transition model. (b) Clock stability estimations. Gray squares: experimental data from dedrifted correction frequencies; black dots: experimental data from in-loop transition probabilities when running the clock; red solid line: data from the clock stability model.

$\gamma = 4.1 \times 10^{-16}$, and $T_c = 0.482$ s are applied to Eq. (2). This gives us a clock stability of $6.3 \times 10^{-16}/\sqrt{\tau}$, which is very close to the experimental measurement. We have performed several rounds of such kinds of measurements and calculations. With these typical experimental parameters, we obtain repeatable stabilities below $7.0 \times 10^{-16}/\sqrt{\tau}$ that are further confirmed by the model. This proves the benefits of the 2D-MOT to the Hg optical lattice clock.

V. CONCLUSION

In conclusion, we have demonstrated, the characterization of a 2D-MOT for Hg. Reliable spectroscopic-grade sources of 254-nm laser light are built to drive the cooling transition of ^{199}Hg . Parameters affecting the efficiency of the 2D-MOT are studied. A gain factor of 4.5 is obtained in the MOT atom loading rate thanks to the 2D-MOT. Moreover,

a repeatable short-term stability of less than 7.0×10^{-16} at 1 s is observed in our Hg clock. The potential of the 2D-MOT might be further explored by optimizing the beam size of the trapping beam and by using the other two trapping zones in the future. The improved atomic number by the 2D-MOT will provide further leverage to study the cold atom collisional shifts and other phenomena in optical lattice clocks.

Note added in proof. Recently, we found a similar work on 2D-MOT for Hg was published in Ref. [34].

ACKNOWLEDGMENTS

C.G. and V.C. contributed equally to the experiment. We acknowledge contributions from the SYRTE electronic workshop. This work was supported by ERC Consolidator Grant AdOC (ERC-2013-CoG-617553).

-
- [1] I. Bloch, J. Dalibard, and W. Zwerger, Many-body physics with ultracold gases, *Rev. Mod. Phys.* **80**, 885 (2008).
- [2] K. Bongs, Y. Singh, L. Smith, W. He, O. Kock, D. Świerad, J. Hughes, S. Schiller, S. Alighanbari, S. Origlia, S. Vogt, U. Sterr, C. Lisdat, R. Le Targat, J. Lodewyck, D. Holleville, B. Venon, S. Bize, G. Barwood, P. Gill *et al.*, Development of a strontium optical lattice clock for the SOC mission on the ISS, *C. R. Phys.* **16**, 553 (2015).
- [3] C. L. Degen, F. Reinhard, and P. Cappellaro, Quantum sensing, *Rev. Mod. Phys.* **89**, 035002 (2017).
- [4] S. Bize, The unit of time: Present and future directions, *C. R. Phys.* **20**, 153 (2019).
- [5] R. Geiger, A. Landragin, S. Merlet, and F. P. D. Santos, High-accuracy inertial measurements with cold-atom sensors, *AVS Quantum Science* **2**, 024702 (2020).
- [6] L. D. Carr, D. DeMille, R. V. Krems, and J. Ye, Cold and ultracold molecules: Science, technology and applications, *New J. Phys.* **11**, 055049 (2009).
- [7] M. S. Safronova, D. Budker, D. DeMille, D. F. J. Kimball, A. Derevianko, and C. W. Clark, Search for new physics with atoms and molecules, *Rev. Mod. Phys.* **90**, 025008 (2018).
- [8] K. Dieckmann, R. J. C. Spreeuw, M. Weidemüller, and J. T. M. Walraven, Two-dimensional magneto-optical trap as a source of slow atoms, *Phys. Rev. A* **58**, 3891 (1998).
- [9] S. Dörscher, A. Thobe, B. Hundt, A. Kochanke, R. Le Targat, P. Windpassinger, C. Becker, and K. Sengstock, Creation of quantum-degenerate gases of ytterbium in a compact 2D-/3D-magneto-optical trap setup, *Rev. Sci. Instrum.* **84**, 043109 (2013).
- [10] I. Nosske, L. Couturier, F. Hu, C. Tan, C. Qiao, J. Blume, Y. H. Jiang, P. Chen, and M. Weidemüller, Two-dimensional magneto-optical trap as a source for cold strontium atoms, *Phys. Rev. A* **96**, 053415 (2017).
- [11] S. Saskin, J. T. Wilson, B. Grinkemeyer, and J. D. Thompson, Narrow-Line Cooling and Imaging of Ytterbium Atoms in an Optical Tweezer Array, *Phys. Rev. Lett.* **122**, 143002 (2019).
- [12] M. Barbiero, M. G. Tarallo, D. Calonico, F. Levi, G. Lamporesi, and G. Ferrari, Sideband-Enhanced Cold Atomic Source for Optical Clocks, *Phys. Rev. Appl.* **13**, 014013 (2020).
- [13] M. Petersen, R. Chicireanu, S. T. Dawkins, D. V. Magalhães, C. Mandache, Y. Le Coq, A. Clairon, and S. Bize, Doppler-Free Spectroscopy of the $^1S_0 - ^3P_0$ Optical Clock Transition in Laser-Cooled Fermionic Isotopes of Neutral Mercury, *Phys. Rev. Lett.* **101**, 183004 (2008).
- [14] H. Hachisu, K. Miyagishi, S. G. Porsev, A. Derevianko, V. D. Ovsiannikov, V. G. Pal'Chikov, M. Takamoto, and H. Katori, Trapping of Neutral Mercury Atoms and Prospects for Optical Lattice Clocks, *Phys. Rev. Lett.* **100**, 053001 (2008).
- [15] J. McFerran, L. Yi, S. Mejri, and S. Bize, Sub-doppler cooling of fermionic Hg isotopes in a magneto-optical trap, *Opt. Lett.* **35**, 3078 (2010).
- [16] P. Villwock, S. Siol, and T. Walther, Magneto-optical trapping of neutral mercury, *Eur. Phys. J. D* **65**, 251 (2011).
- [17] J. Paul, Y. Kaneda, T.-L. Wang, C. Lytle, J. V. Moloney, and R. J. Jones, Doppler-free spectroscopy of mercury at 253.7 nm using a high-power, frequency-quadrupled, optically pumped external-cavity semiconductor laser, *Opt. Lett.* **36**, 61 (2011).
- [18] H.-L. Liu, S.-Q. Yin, K.-K. Liu, J. Qian, Z. Xu, T. Hong, and Y.-Z. Wang, Magneto-optical trap for neutral mercury atoms, *Chin. Phys. B* **22**, 043701 (2013).
- [19] M. Witkowski, B. Nagórny, R. Munoz-Rodriguez, R. Ciuryło, P. S. Żuchowski, S. Bilicki, M. Piotrowski, P. Morzyński, and M. Zawada, Dual Hg-Rb magneto-optical trap, *Opt. Express* **25**, 3165 (2017).
- [20] Q. Lavigne, T. Groh, and S. Stellmer, Magneto-optical trapping of mercury at high phase-space density, *Phys. Rev. A* **105**, 033106 (2022).
- [21] J. Boulet, R. Bello-Doua, R. Dubrasquet, N. Traynor, C. Lecaplain, A. Hideur, J. Lhermite, G. Machinet, C. Médina, and E. Cormier, Visible and Infrared Sources based on Three-Level Ytterbium-doped Fiber Lasers, *Fiber Laser Applications, FThC5* (Optical Society of America, Washington DC, 2011).
- [22] S. Mejri, J. J. McFerran, L. Yi, Y. Le Coq, and S. Bize, Ultraviolet laser spectroscopy of neutral mercury in a one-dimensional optical lattice, *Phys. Rev. A* **84**, 032507 (2011).
- [23] M. Petersen, Laser-cooling of neutral mercury and laser-spectroscopy of the $^1S_0 - ^3P_0$ optical clock transition, Ph.D thesis, Université Pierre-et-Marie-Curie, 2009, <https://theses.hal.science/tel-00405200>.
- [24] M. Witkowski, G. Kowzan, R. Munoz-Rodriguez, R. Ciuryło, P. S. Żuchowski, P. Masłowski, and M. Zawada, Absolute frequency and isotope shift measurements of mercury $^1S_0 - ^3P_1$ transition, *Opt. Express* **27**, 11069 (2019).
- [25] R. Tyumenev, M. Favier, S. Bilicki, E. Bookjans, R. L. Targat, J. Lodewyck, D. Nicolodi, Y. L. Coq, M. Abgrall, J. Guéna, L. D. Sarlo, and S. Bize, Comparing a mercury optical lattice clock with microwave and optical frequency standards, *New J. Phys.* **18**, 113002 (2016).
- [26] N. Bucalovic, V. Dolgovskiy, C. Schori, P. Thomann, G. Di Domenico, and S. Schilt, Experimental validation of a simple approximation to determine the linewidth of a laser

- from its frequency noise spectrum, *Appl. Opt.* **51**, 4582 (2012).
- [27] G. Santarelli, P. Laurent, P. Lemonde, A. Clairon, A. G. Mann, S. Chang, A. N. Luiten, and C. Salomon, Quantum Projection Noise in an Atomic Fountain: A High Stability Cesium Frequency Standard, *Phys. Rev. Lett.* **82**, 4619 (1999).
- [28] G. J. Dick, Local oscillator induced instabilities in trapped ion frequency standards, in *Proceedings of 19th Annual Precise Time and Time Interval Meeting, Redondo Beach, 1987* (U.S. Naval Observatory, 1989), pp. 133–147.
- [29] A. Quessada, R. P. Kovacich, I. Courtillot, A. Clairon, G. Santarelli, and P. Lemonde, The dick effect for an optical frequency standard, *J. Opt. B: Quantum Semiclassical Opt.* **5**, S150 (2003).
- [30] C. Guo, M. Favier, N. Galland, V. Cambier, H. Álvarez-Martínez, M. Lours, L. De Sarlo, M. Andia, R. Le Targat, and S. Bize, Accurate laser frequency locking to optical frequency combs under low-signal-to-noise-ratio conditions, *Rev. Sci. Instrum.* **91**, 033202 (2020).
- [31] M. Favier, Mercury optical lattice clock: From high-resolution spectroscopy to frequency ratio measurements, Ph.D thesis, Université Pierre-et-Marie-Curie, 2017, <https://hal.archives-ouvertes.fr/tel-01636177>.
- [32] V. Cambier, Mercury atom optical lattice clock using 2D-MOT: 3P_0 state lifetime and frequency measurements, Ph.D. thesis, Sorbonne Université, 2019, <https://hal.archives-ouvertes.fr/tel-02501535>.
- [33] J. J. McFerran, D. V. Magalhães, C. Mandache, J. Millo, W. Zhang, Y. Le Coq, G. Santarelli, and S. Bize, Laser locking to the $^{199}\text{Hg } ^1S_0 - ^3P_0$ clock transition with $5.4 \times 10^{-15}/\sqrt{\tau}$ fractional frequency instability, *Opt. Lett.* **37**, 3477 (2012).
- [34] Y. Zhang, Q.-X. Liu, J.-F. Sun, Z. Xu, and Y.-Z. Wang, Enhanced cold mercury atom production with two-dimensional magneto-optical trap, *Chin. Phys. B* **31**, 073701 (2022).